Spin-induced shape changes in light-medium mass compound nuclei

Z. M. Drebi,* K. A. Snover, A. W. Charlop,† M. S. Kaplan,† D. P. Wells,‡ and D. Ye§
Nuclear Physics Laboratory, University of Washington, Seattle, Washington 98195

Y. Alhassid
A. W. Wright Nuclear Structure Laboratory, Yale University, New Haven, Connecticut 06511
(Received 16 March 1995)

At very high spins an oblate-to-triaxial transition in the equilibrium shape of hot medium mass nuclei is expected, with superdeformed major to minor axis ratios of 2:1 and larger. To search for this shape transition, we measured γ ray production cross sections and angular distributions for the decay of ^{59,63}Cu compound nuclei populated in the fusion of ^{32}S+^{27}Al and ^{18}O+^{45}Sc over a wide range of spin ($J = 0 - 47\hbar$) and excitation energy ($E^* = 55$–130 MeV). Very broad giant dipole resonance (GDR) strength functions are deduced at high bombarding energy (spin), implying the existence of large deformation in the ensemble of decaying states. Thermal shape and orientation fluctuation calculations based on the rotating liquid drop model provide a good description of the GDR strength functions for all cases. The calculations fail to reproduce the GDR strength functions at high bombarding energy (spin) when the oblate-to-triaxial shape transition and the associated softness in the potential energy surface are removed, indicating the observed broadening of the GDR strength function is due mostly to spin-driven deformation. Threshold bremsstrahlung production is inferred from measured angular distribution anisotropies in ^{18}O+^{45}Sc collisions at 125 and 149 MeV.

PACS number(s): 24.30.Cz, 23.20.−g, 25.70.Gh, 27.50.+e

I. INTRODUCTION

An outstanding question in nuclear physics is the nature of the equilibrium shape of the nucleus at high excitation energies and at angular momenta near the limit of what a nucleus can sustain. The rotating liquid-drop model (RLDM) [1–3] predicts the nucleus should experience a shape transition, at very high spins, from an oblate noncollective shape to a triaxial (approximately prolate collective) shape, with superdeformed major to minor axis ratios of 2:1 and larger. In light and medium mass nuclei, these highly deformed triaxial shapes are predicted to exist as equilibrium shapes of the rapidly rotating nucleus. In an infinite system this shape change is a second-order phase transition similar to the Jacobi shape instability in gravitating rotating stars.

The experimental investigation of the shapes and shape evolution of hot rotating nuclei at very high excitation energy and spin has been possible through studies of giant dipole resonance (GDR) γ decays of compound nuclei formed in heavy-ion fusion reactions [4,5]. Both the GDR spectrum shape and angular distribution are sensitive to nuclear deformation. In a deformed nucleus, the GDR splits into components corresponding to vibrations along the different principal nuclear axes. The fractional energy splitting is proportional to the fractional difference in the axes lengths, which is simply related to the nuclear deformation. In hot nuclei, the energy splitting of the GDR is usually not resolvable, in part because of thermal shape fluctuations. In order to infer quantitative information about the equilibrium nuclear shape and shape evolution from GDR data, comparison with full thermal fluctuation calculations is necessary. Excited-state GDR spectroscopy has established itself as a powerful method to study nuclear shapes at high temperature and spin (see, for example, [6,7]).

In this paper, we present GDR energy spectra and angular distribution measurements for decays of excited ^{59}Cu and ^{63}Cu compound nuclei populated over a wide range of spin ($J = 0$–$47\hbar$) and excitation energy ($E^* = 55$–130 MeV) in the fusion of ^{32}S+^{27}Al and ^{18}O+^{45}Sc. Our goal is to search for the highly deformed nuclear shapes associated with the predicted spin-induced oblate-to-triaxial transition. The compound nuclei studied lie in the mass region where highly deformed triaxial shapes are expected to be most pronounced [1]. In addition, measured fusion cross sections for ^{32}S+^{27}Al in our range of study imply spin distributions which extend significantly beyond the critical spin calculated for the oblate-triaxial shape transition. Our main experimental result is the determination of the shape and the width of the GDR as a function of nuclear spin and temperature. We find good agreement between the experimentally determined shape of the GDR and the prediction

*Present address: Physics Department, University of Al-Fateh (Tripoli), Tripoli, Libya.
†Present address: Medical Center, Department of Radiology, University of Washington, Seattle, WA 98195.
‡Present address: Environmental Radiation Section, Department of Health, Radiation Protection Division, Air Industrial Park, Bldg. 5, P.O. Box 47827, Olympia, WA 98504.
§Present address: University of Chicago, Chicago, IL 60637.

of the thermal fluctuation theory only when the oblate-to-triaxial shape transition is included in the calculations. Recently, similar results have been reported for excited ^{45}Sc compound nuclei [6]. Compared to [6], the main advantage of the present study is the examination of both mass-symmetric and mass-asymmetric reactions, which permits a much better understanding of possible backgrounds, including nuclear bremsstrahlung. For ^{18}O+^{45}Sc, angular distribution measurements at the highest bombarding energies, 125 and 149 MeV, were used to determine the bremsstrahlung cross section near threshold, where bremsstrahlung and GDR decay cannot be resolved in the total cross section, but may be distinguished in the angular distribution.

The experimental details are described in Sec. II. In Sec. III, the experimental results are presented and background corrections are discussed. Statistical model analysis is discussed in Sec. IV. The experimental results are compared to thermal shape fluctuation calculations in Sec. V and a conclusion is given in Sec. VI.

II. EXPERIMENTAL DETAILS

Measurements of γ rays from ^{32}S+^{27}Al and ^{18}O+^{45}Sc collisions, each at five different bombarding energies in the range 90–215 and 54–149 MeV, respectively, were performed at the University of Washington Nuclear Physics Laboratory using the tandem-injected superconducting linac (see Table I). Inclusive high-energy γ-ray singles spectra and angular distributions were measured for all the reactions. Coincidence data in which the γ multiplicity was also measured using a multiplicity filter were taken for three of the reactions, 175 and 215 MeV ^{32}S+^{27}Al and 125 MeV ^{18}O+^{45}Sc. Self-supporting rolled metallic foils of natural ^{27}Al and natural ^{45}Sc (chemical purity 99.99%) were used as targets. Carbon buildup was kept to a negligible level by use of a liquid-nitrogen cold shroud surrounding the target. Target oxidization was measured to be negligible (<0.2%) using the ^{16}O$(p,p'\gamma)$ reaction.

A. NaI spectrometer

High-energy γ rays were detected with a NaI spectrometer consisting of a large cylindrical NaI(Tl) crystal 38 cm long and 25 cm in diameter surrounded by an active plastic anticoincidence shield, and passive ^{6}LiH and lead shielding. The plastic shield serves primarily to reject cosmic rays; it also improves the detector energy resolution by rejecting events which deposit part of their energy in the shield. Long-term gain stability of the NaI spectrometer of better than 0.5% over a period of a week was achieved using a stabilized LED feedback circuit. The energy calibration was performed in the range $E_\gamma = 2.9$–22.6 MeV using the ^{11}B$(p,\gamma)^{12}$C and ^{11}B$(p,p'\gamma)^{11}$B reactions. The front face of the lead detector collimator was positioned 49 cm from the target. The absolute detector efficiency at $E_\gamma = 15.1$ MeV was deduced from the known yield of the lowest $T = \frac{3}{2}$ resonance in the ^{12}C$(p,\gamma_0)^{13}$N reaction at $E_p = 14.2$ MeV [8]. In the inclusive γ-ray measurements, the energy threshold in the plastic anticoincidence shield was set at 10–20 keV, and a wax absorber of 36 cm thickness was placed between the detector and the target. In the coincidence measurements, 11 cm of wax was used, and the plastic threshold was set to 400 keV. The resulting measured efficiency solid angle product for a 90–110% window set around the photopeak at $E_\gamma = 15.1$ MeV was measured to be $\varepsilon d\Omega = 8.7 \pm 0.3$ and 21.7 ± 0.7 msr for the inclusive and coincidence setups, respectively. The energy dependence of the efficiency is based on the work of Glatzel [9] and is shown in Fig. 1 for the two setups. The detector line shape was measured at $E_\gamma = 22.6$ MeV in the ^{11}B$(p,\gamma)^{12}$C reaction, and obtained at other energies in the good approximation that the line shape depends only on the ratio E/E_γ, where E is the detected energy. The line shape and the efficiency were folded into CASCADE statistical model calculations for comparison to measured spectra. Time of flight was used with a pulsed beam (240-nsec repetition rate) to eliminate neutron background, and standard techniques were employed to reduce pulse pileup.

B. Multiplicity filter

The γ multiplicity filter (MF) is an array of 23 cylindrical NaI detectors 7.6 cm diameter and 10.2 cm long, with their front faces 15.2 cm from the center of the target, mounted on a spherical structure [10]. The product of the solid angle and efficiency for each detector was determined to be 0.8% at $E_\gamma = 1$ MeV, corresponding to 18.4% for all 23 detectors. The detectors were wrapped with a 3.2 mm lead shield on the sides, which reduced the Compton cross talk to less than 3%. Because the high-

TABLE I. Reaction parameters.

^{18}O+^{45}Sc				^{32}S+^{27}Al			
E_p (MeV)	$(E_p - V_p)/A_p$ (MeV/nucleon)	E^* (MeV) [a]	$2I_0\hbar/3$ [b]	E_p (MeV)	$(E_p - V_p)/A_p$ (MeV/nucleon)	E^* (MeV) [a]	$2I_0\hbar/3$ [b]
52	0.98	61.1	17.3	90	0.74	54.4	15.0
68	1.98	72.4	23.3	120	1.68	68.1	22.4
105	3.93	99.1	25.3	141	2.34	77.7	26.5
125	5.04	113.0	25.3	175	3.40	93.2	28.7
149	6.37	130.1	25.3	215	4.65	111.4	30.7

[a] Compound nucleus excitation energy.
[b] Average compound nucleus angular momentum.

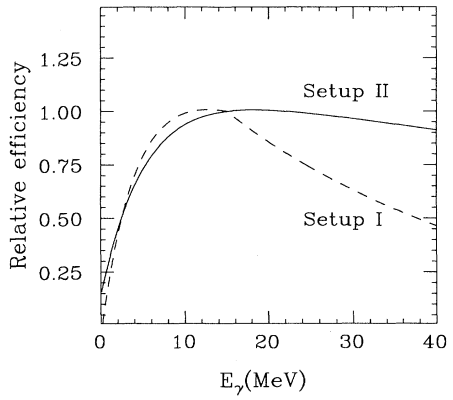

FIG. 1. Relative detection efficiency for two different combinations of shielding and veto threshold.

energy γ-ray production cross section is small, a typical event rate $\sim$ 0.5 kHz ($E_\gamma > 7$ MeV) in the large NaI spectrometer resulted in a large, $\sim$ 80 kHz singles rate in the individual MF detectors. This required the use of transistorized photomultiplier (PM) bases which were stable at high counting rate. The pulses from the PM bases were clipped to a length of 250 nsec, to reduce pileup, using passive RL shaping. Because of problems with gain deterioration when the Hamamatsu R1911 phototubes were operated at normal high voltage ($\sim$ 1200 V), the bases were operated at 700–800 V and $\times$100 gain amplification was used in the pulse processing. Constant fraction discrimination with a 100-keV threshold was used to generate timing signals, and time-to-digital converters were used to register the time of flight between the large NaI trigger and the individual MF detectors. The time-of-flight measurements were made over a 500-nsec period in order to record the random detection of MF events in the following beam burst, which was used to compute randoms corrections for events involving two or more compound nuclei reactions in the prompt beam burst.

III. EXPERIMENTAL RESULTS

A. Inclusive γ-ray measurements

Inclusive γ-ray energy spectra at each bombarding energy for the two systems studied, ^{32}S+^{27}Al and ^{18}O+^{45}Sc, were measured at the laboratory angles θ_γ = 40°, 55°, 90°, 125°, and 140°, and then transformed to the compound nucleus (CN) center-of-mass frame. The center-of-mass angular distributions were fitted with a Legendre polynomial expansion

$$W(\theta) = A_0[1 + a_1 P_1(\cos\theta) + a_2 P_2(\cos\theta)] .$$

The total inclusive γ-ray cross sections, obtained from an average over all angles, and the extracted angular distribution coefficients $a_1(E_\gamma)$ are shown in Figs. 2 and 3, respectively. The solid curves on the spectral shapes are statistical model fits to the data discussed in Sec. IV. The measured $a_2(E_\gamma)$ coefficients are presented in Sec. V together with the results of the thermal fluctuation calculations.

The $a_1(E_\gamma)$ coefficients provide an independent check of the statistical nature of the emitted γ rays, since forward-backward symmetry in the center-of-mass frame is required for statistical decay, and hence $a_1(E_\gamma)$ must be zero. In the ^{32}S+^{27}Al, $a_1(E_\gamma)$ is consistent with zero in the GDR region of interest $12 < E_\gamma < 30$ MeV, for all five bombarding energy cases, supporting the compound nucleus decay hypothesis. However, for $E_p \geq 120$ MeV and $E_\gamma \leq 12$ MeV, large negative $a_1(E_\gamma)$ values are found, together with an excess in the measured γ-ray yield relative to the statistical model predictions.

For ^{18}O+^{45}Sc the measured $a_1(E_\gamma)$ coefficients are consistent with zero only for the 52- and 68-MeV cases. At higher bombarding energy, deviations from CN statistical emission are evident in different regions of the energy spectrum: $E_\gamma \leq 12$ MeV where positive $a_1(E_\gamma)$ coefficients are observed, near $E_\gamma = 15$ MeV, and in the high-energy region $E_\gamma > 22$ MeV. Possible sources of background associated with these departures of $a_1(E_\gamma)$ from zero are discussed in the next section.

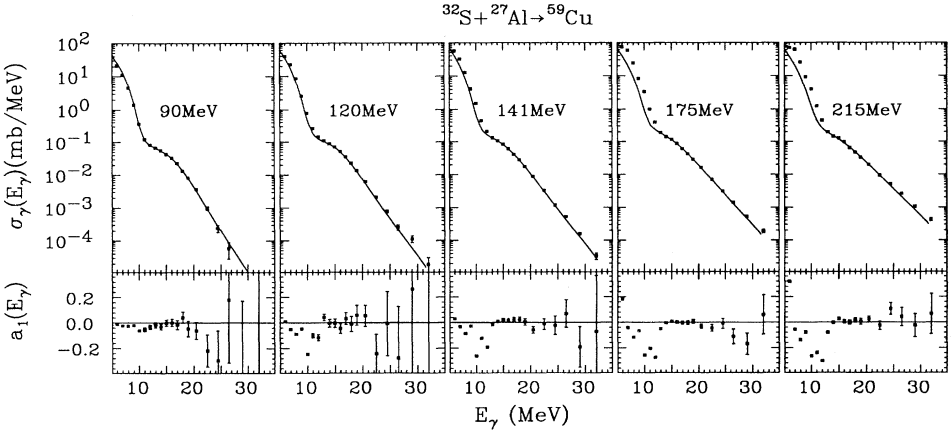

FIG. 2. Inclusive γ-ray production cross sections $\sigma_{\rm abs}(E_\gamma)$ (top row), and $a_1(E_\gamma)$ (bottom row) for ^{32}S+^{27}Al. The solid curves are CASCADE fits to the measured cross sections, as discussed in Sec. IV.

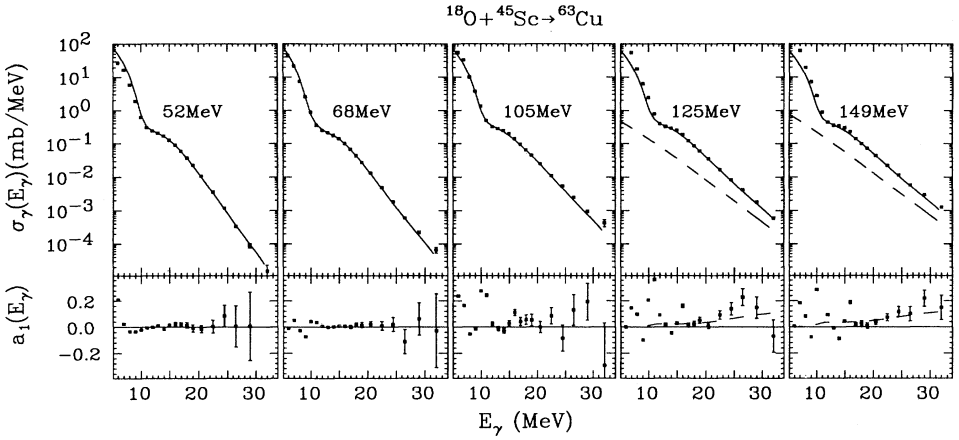

FIG. 3. $^{18}O+^{45}Sc$ results, as in Fig. 2. For the 125- and 149-MeV cases, the dashed curves represent the bremsstrahlung contribution (see text) and the solid curves represent the sum of the bremsstrahlung and statistical contributions. The cross sections for the 105-, 125-, and 149-MeV cases have been corrected for the 15.1-MeV line (see text), while $a_1(E_\gamma)$ has not been corrected.

B. Background from nonstatistical processes

Inelastic scattering and transfer reactions populating low-energy states are important even at low bombarding energy. As the bombarding energy increases, in medium mass systems the fusion-evaporation cross section saturates, typically around E_p/A_p = 3–5 MeV/nucleon, where E_p is the projectile bombarding energy and A_p is the projectile mass, and other reactions such as deep inelastic scattering and fusion-fission become important. Nuclear bremsstrahlung, though not normally expected at our bombarding energies, turns out to be important. Of these processes, typically only nuclear bremsstrahlung and γ decay following deep-inelastic or fusion fission can have large enough cross sections to contribute significantly to the high-energy γ-ray yield. The exception is excitation and decay of the 15.1-MeV state in ^{12}C. Background from these sources is discussed in subsections 1–4 below. The issue of preequilibrium emission prior to CN formation is discussed in Sec. IV C.

1. Deep-inelastic background

We have estimated the cross section for production of γ rays from decay of excited fragments produced in deep-inelastic collisions (plus fusion fission) of 175 MeV $^{32}S+^{27}Al$. The production cross section, excitation energy, and spin of the fragments were first determined. For estimation purposes, we used an upper limit to the binary reaction cross section given by the difference of the measured total reaction cross section [11,12] and the measured fusion-evaporation cross section [13]. For E_p = 175 MeV this limit is $\approx$ 700 mb. The excitation energy distribution of the fragments was estimated from the measured primary Q-value distributions of deep-inelastic scattering of $^{32}S+^{27}Al$ at E_p = 135–190 MeV [14,15]. We assumed that the excited fragments reach thermal equilibrium prior to decay. As a result, the excitation energy in the projectilelike and targetlike fragments is divided proportional to their masses. A rough estimate of the angular momentum involved in the deep-inelastic (DI) reaction can be obtained from the fusion and total (fusion plus binary) cross sections assuming a sharp cutoff approximation for both spin distributions. For 175 MeV $^{32}S+^{27}Al$ the result is $\langle l\rangle_{DI} \approx 50\hbar$. In the rolling or sticking rigid-body limits (these two limits are similar for near-symmetric systems) the average fragment spin is $\langle l\rangle_{DI}/7 \approx 7\hbar$. CASCADE calculations were performed for γ decay of both targetlike and projectilelike fragments, with ^{27}Al and ^{32}S chosen as representative fragments. The CASCADE calculations for each fragment were averaged over the excitation energy (Q-value) distributions which correspond for 175 MeV ^{32}S and ^{27}Al to a mean excitation energy of $\approx$ 20 MeV for each fragment. The sum of the calculated γ-ray spectra from decay of both fragments is plotted in Fig. 4 (dashed line) along with the measured γ-ray production cross section and the CASCADE calculation of the contribution from compound nuclear decay (solid line). The deep-inelastic contribution to the GDR region is negligible. For E_γ < 10 MeV the shape of the calculated deep-inelastic contribution is similar to the measured total yield; however, the magnitude is a factor of 5–10 smaller than the observed excess in the measured yield relative to the calculated compound nucleus contribution. Similar calculations for other representative fragments were performed with similar results.

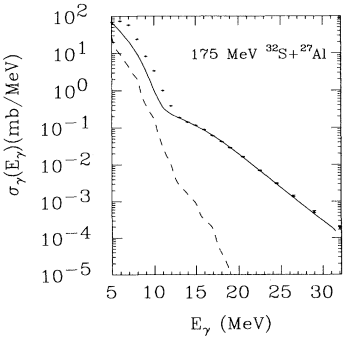

FIG. 4. Calculated γ-ray production cross section from deep-inelastic scattering (dashed curve), and from compound nucleus decay (solid curve) for 175 MeV $^{32}S+^{27}Al$. Data points are the measured inclusive cross section.

In the above analysis, we have assumed that the decay of the excited binary fragments is statistical. For deep-inelastic scattering this is generally believed to be the case. For example, in 156 MeV ^{32}S+^{64}Ni and 143 MeV ^{28}Si+^{64}Ni reactions, the γ-ray spectra, measured in coincidence with deep-inelastic fragments, were found to be statistical [16]. However, for 143 MeV ^{32}S+^{64}Ni collisions, nonstatistical γ rays were found to dominate the emission spectra from the excited fragments [17].

2. *Nuclear bremsstrahlung*

At bombarding energies $E_p/A_p \geq 10$–15 MeV/nucleon, heavy-ion collisions produce high-energy γ rays via the process of nuclear bremsstrahlung [18]. Bremsstrahlung is observed as an exponentially falling component in the γ-ray spectrum at high γ-ray energy, $E_\gamma \geq 30$ MeV, extending beyond the statistical component and understood as arising from collisions of individual protons in the projectile with neutrons in the target and vice versa. The emission is characterized by forward-backward symmetry [$a_1(E_\gamma) = 0$] in a reference frame moving with half the projectile velocity—the "nucleon-nucleon center of mass." A universal dependence of the cross section on $(E_p - V_p)/A_p$ is observed, where V_p is the Coulomb barrier energy. The cross section is usually parametrized as $\sigma_\gamma^{\rm brem}(E_\gamma) = \sigma_0 \exp(-E_\gamma/E_0)$, where σ_0 and E_0 depend on $(E_p - V_p)/A_p$. In the low-energy regime $E_p/A_p \leq 10$–15 MeV/nucleon, the cross section σ_0 drops very rapidly with decreasing E_p/A_p, and the inverse slope parameter E_0 also drops. At bombarding energies between threshold and 10 MeV/nucleon or so, the bremsstrahlung cross section will not be resolved from the high E_γ tail due to statistical emission. At such low bombarding energies, $\sigma_\gamma^{\rm brem}(E_\gamma)$ should be observable in mass-asymmetric collisions as a forward-backward asymmetry in the nucleus-nucleus center of mass. This is because, in such collisions, $v_p/2 \neq v_{\rm CN}$, so that bremsstrahlung will be asymmetric in the nucleus-nucleus center of mass, while the CN component is required to be symmetric. For mass-asymmetric collisions with light projectile and heavy target, the $a_1(E_\gamma)$ which would result from bremsstrahlung alone should be positive, and should increase with E_γ at a fixed bombarding energy, and should increase with E_p at a fixed E_γ. The observed $a_1(E_\gamma)$ will be diluted by statistical decay, which is forward-backward symmetric in the center of mass. Since the fraction of the cross section due to statistical decay should drop with increasing E_γ, the effect of this dilution will be to increase the rate of change of $a_1(E_\gamma)$ with E_γ over that which would result from pure bremsstrahlung alone. These trends are consistent with the measured ^{18}O+^{45}Sc data, Fig. 3, where it is seen for $E_\gamma > 20$ MeV, $a_1(E_\gamma) \cong 0$ for $E_p \leq 105$ MeV, and $a_1(E_\gamma)$ is nonzero and increasing with E_γ for $E_p \geq 125$ MeV.

We have estimated the bremsstrahlung cross section for the two cases where it is observed, 125 and 149 MeV ^{18}O+^{45}Sc. The cross section is assumed to fall exponentially as given above. The proportionality constant σ_0 and the slope parameter E_0 cannot be obtained by extrapolating the bremsstrahlung systematics which are known for systems with higher bombarding energies, to our lower bombarding energies, because of the steep fall of the measured integrated cross sections at low $(E_p - V_p)/A_p$ [18]. Also, no theoretical model can be used to calculate σ_0 or E_0 reliably at these energies. Instead, we treated σ_0 and E_0 as free parameters, determined by fitting the observed angular distribution $a_1(E_\gamma)$ coefficients. In this process, the bremsstrahlung cross section, assuming isotropic emission in the nucleon-nucleon center-of-mass frame, was calculated with starting values for σ_0 and E_0, transformed to the CN center-of-mass frame, and then $a_1^{\rm brem}(E_\gamma)$ was determined by fitting the calculated bremsstrahlung angular distribution. The calculated $a_1(E_\gamma)$ was obtained by multiplying $a_1^{\rm brem}(E_\gamma)$ by the compound nuclear dilution factor obtained from the ratio of the estimated bremsstrahlung cross section to the measured cross section (bremsstrahlung plus statistical). This process was iterated, adjusting the free parameters σ_0 and E_0 so as to obtain agreement between the measured and calculated $a_1(E_\gamma)$. In Fig. 3, we show, for the 125 and 149 MeV ^{118}O+^{45}Sc cases, the bremsstrahlung contribution (dashed curve) determined in this manner. The fitted parameters are $\sigma_0 = 1.5 \pm 0.3$ mb/MeV and $E_0 = 3.9 \pm 0.2$ MeV^{-1} for $E_p = 125$ MeV, and $\sigma_0 = 2.4 \pm 0.4$ mb/MeV and $E_0 = 4.0 \pm 0.2$ MeV^{-1} for $E_p = 149$ MeV. In the next step, $\sigma_\gamma^{\rm brem}(E_\gamma)$ was added to the CASCADE statistical model calculation of the CN contribution, and the GDR parameters were obtained by a χ^2 fit to the measured cross section as discussed in Sec. IV. The result is shown as the solid curves in Fig. 3 for the $E_p = 125$ and 149 MeV cases. According to this analysis, bremsstrahlung contributes from about 15 ± 5 to 50 ± 10% of the total measured yield in the energy range 15–30 MeV for the $E_p = 149$ MeV case. The large quoted E^γ uncertainty in our bremsstrahlung estimate reflects the statistical errors of the measured $a_1(E_\gamma)$ at high E_γ.

The mass asymmetry of the ^{18}O+^{45}Sc system permits identifying and correcting for the nucleon-nucleon bremsstrahlung since, as discussed above, the nucleon-nucleon and compound nucleus center-of-mass velocities are different. This identification is not possible in the near-symmetric ^{32}S+^{27}Al system. However, the ^{18}O+^{45}Sc results suggests that the onset of nucleon-nucleon bremsstrahlung emission takes place at $125 > E_p > 105$ MeV corresponding to $5.0 > (E_p - V_p)/A_p > 3.9$ MeV/nucleon (Table I). If we assume that the bremsstrahlung yield scales according to $(E_p - V_p)/A_p$, as is suggested by the known nucleon-nucleon bremsstrahlung systematics [18], then the bremsstrahlung in $E_p \leq 175$ MeV ^{32}S+^{27}Al, which corresponds to $(E_p - V_p)/A_p \leq 3.4$ MeV/nucleon, should be negligible, while the $E_p = 215$ MeV ^{32}S+^{27}Al case, which corresponds to $(E_p - V_p)/A_p = 4.7$ MeV/nucleon, lies in the threshold region of bremsstrahlung onset. Recently the bremsstrahlung yield has been found to be greater in systems with a neutron excess [19]. This suggests that at the same $(E_p - V_p)/A_p$, the bremsstrahlung cross section for ^{32}S+^{27}Al collisions should be smaller than for ^{18}O+^{45}Sc collisions. Hence bremsstrahlung in the 215 MeV ^{32}S+^{27}Al cases should be small also.

3. The 15.1-MeV emission line

A γ-ray line near 15 MeV is present in the $^{18}O+^{45}Sc$ γ-ray energy spectra at $E_p = 105$, 125, and 149 MeV. The line can be seen in Fig. 5, which displays a portion of a $\theta_\gamma = 90°$ spectrum from $^{18}O+^{45}Sc$ at 125 MeV. This line is most likely the $M1$ γ transition from the 15.1 MeV, $1^+, T = 1$ state to the ground state in ^{12}C. The reason is that, besides agreeing in energy with this assignment, this transition has an unusually high absolute branching ratio (88%) [20] for a high-energy γ-ray transition. Hence excited ^{12}C nuclei may be populated by projectile breakup or particle transfer with a very small population cross section (≈ 0.06 mb for $E_p = 125$ MeV) and produce a noticeable 15.1 line. The angular distribution of this line was found to be forward peaked in the CN center-of-mass frame, suggesting that the mechanism for $^{12}C^*$ production is projectilelike excitation.

The measured spectra at each angle were corrected for this line in the following procedure. The emission line spectrum at 90° was obtained by subtracting from the measured spectrum a CASCADE fit obtained by excluding a narrow region around 15 MeV. We assumed this line spectrum was emitted from a reference frame moving along the beam axis with a fixed velocity—the "source reference frame." Assuming isotropic emission in the source reference frame, the emission line spectra, shape and magnitude, were calculated at the other angles using the Lorentz transformation. The source velocity was obtained by comparing the resulting Doppler-shifted spectra with the observed line spectra at the other four angles. For all three bombarding energies, the best results were obtained with a source velocity $v_s = 0.9v_p$. The calculated emission spectra were then subtracted from the measured spectra at each angle. A corrected spectrum obtained in this fashion is shown in Fig. 5, along with the corrected and uncorrected $a_1(E_\gamma)$ coefficients. The uncorrected $a_1(E_\gamma)$ shows a dispersionlike shape in the vicinity of 15 MeV due to the Doppler-shifted 15.1-MeV line. The absence of this shape in the corrected $a_1(E_\gamma)$ provides a measure of the subtraction accuracy at forward and backward angles. CASCADE fits for these 3 cases discussed in Sec. IV and shown in Fig. 3 were performed to the corrected data.

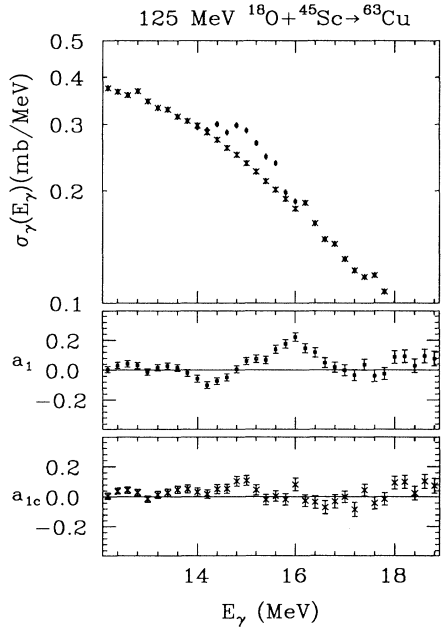

FIG. 5. A typical $\theta_\gamma = 90°$ spectrum from 125 MeV $^{18}O+^{45}Sc$ showing both corrected (crosses) and uncorrected (solid points) spectra and $a_1(E_\gamma)$ coefficients in the vicinity of the 15.1-MeV line.

4. Low-energy background

Below $E_\gamma = 12$ MeV there is a large noncompound nucleus contribution to the measured spectra for $E_p \geq 100$ MeV in both reactions. This component is evident from the nonzero $a_1(E_\gamma)$ coefficients and from the excess of the yield relative to the statistical model calculations. From the sign of the corresponding $a_1(E_\gamma)$ coefficients one concludes that the emission sources in the CN center-of-mass frame are predominantly moving forward in the $^{18}O+^{45}Sc$ case and backward in the $^{32}S+^{27}Al$ case, which indicates predominantly "projectilelike" excitations in $^{18}O+^{45}Sc$ and "targetlike" excitations in $^{32}S+^{27}Al$. Moreover, the structure apparent in $a_1(E_\gamma)$ in this energy region suggests the decay of isolated or semiisolated levels.

Deep-inelastic scattering produces γ-ray background for $E_\gamma \leq 12$ MeV, although apparently not enough to explain the observed cross sections (Fig. 4). This statement needs to be qualified. The decays following DI scattering were calculated for representative fragments masses, using CASCADE with the Reisdorf level density at low excitation energies (see Sec. IV). It is possible that an improvement in this description, such as using measured γ-decay branching ratios and the actual density of individual levels for residual nuclei at low excitation energies, might result in larger calculated γ-production cross sections for $E_\gamma \leq 12$ MeV. However, such improvements are unlikely to affect significantly the calculated cross sections at higher E_γ.

Transfer reactions can also lead to emission of low-energy γ rays with nonzero $a_1(E_\gamma)$ coefficients. Under the assumption that projectilelike and targetlike products are peaked forward and backward, respectively, in the CN center-of-mass frame, γ decay of excited residual nuclei produced in pickup and stripping reactions should result in positive and negative $a_1(E_\gamma)$ coefficients, respectively. Which reaction channels dominate will be influenced by the transfer probabilities and by the binding energies of the residual nuclides which are produced. For example, of the projectilelike and targetlike nuclides that could be produced in $^{32}S+^{27}Al$ collisions, ^{28}Si is bound up to relatively high excitation energy of 10 MeV. Thus, if ^{28}Si is produced strongly and primarily as a targetlike reaction product, then γ decay with $E_\gamma \sim 10$ MeV will produce large negative $a_1(E_\gamma)$ coefficients, as is observed.

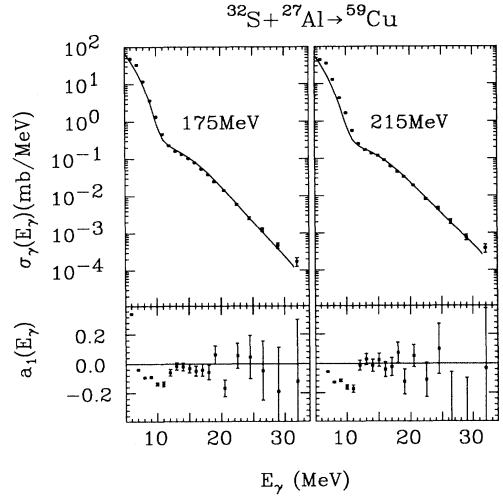

FIG. 6. Cross sections and $a_1(E_\gamma)$ coefficients obtained with a fold $\geq$ 2 condition in the multiplicity filter. Solid curve, CASCADE fits to the measured spectra.

C. Coincidence γ-ray measurements

Coincidence measurements using a multiplicity filter array were carried out for 175 and 215 MeV $^{32}S+^{27}Al$, and 125 MeV $^{18}O+^{45}Sc$ reactions. In these measurements the high-energy γ rays were measured in the large NaI spectrometer in coincidence with the low-energy γ-ray multiplicity. The angular distributions for the 175 MeV $^{32}S+^{27}Al$ case were taken at θ_γ = 40°, 55°, 90°, 125°, and 140°. For the 215 MeV $^{32}S+^{27}Al$ and 125 MeV $^{18}O+^{45}Sc$ cases, data were measured at 40°, 90°, and 140°. The measured cross sections were transformed to the CN center of mass and fitted with a Legendre polynomial expansion, as in the inclusive measurements. The γ-ray energy spectrum at each angle was obtained by requiring a condition of fold $\geq$ 2 on the true fold distribution in the multiplicity filter, where fold is the number of multiplicity filter elements triggered in a given event. The true fold distribution was obtained from the measured fold distribution after correcting for random coincidences. For our reactions, the detection efficiency was 33–40 % with the fold $\geq$ 2 condition.

The spectral shapes and the deduced angular distribution coefficients $a_1(E_\gamma)$ for 175 and 215 MeV $^{32}S+^{27}Al$ reactions are shown in Fig. 6. The solid curves on the spectra are statistical model CASCADE fits. The result of the fold $\geq$ 2 condition is the reduction of the noncompound nucleus yield at $E_\gamma \leq$ 12 MeV by a factor of 2 or so in all cases, with no measurable effect at γ-ray energies above 12 MeV. The $a_1(E_\gamma)$ was also reduced in the region below $E_\gamma \approx$ 12 MeV by about a factor of 2 compared to the inclusive data. At higher γ-ray energies $E_\gamma \geq$ 12 MeV the $a_1(E_\gamma)$ coefficients are consistent with zero, as is the case for the inclusive data.

IV. STATISTICAL MODEL ANALYSIS

We extracted the GDR strength functions by fitting the experimental total cross sections with the statistical model code CASCADE. In all our calculations, we used a version of CASCADE [21] modified to include effects of isospin and parity [22] and including the option of using the Reisdorf level density formula [23, see below]. In CASCADE the cross section $\sigma_{abs}(E_\gamma)$ for the inverse process of GDR photoabsorption [4] was approximated by one Lorentzian with three parameters: the strength (in units of the classical dipole sum rule), resonance energy, and width. One Lorentzian was found to be adequate to fit all of the present data. In fitting the data the Lorentzian parameters were varied simultaneously in a χ^2 fitting procedure in which the parameter space was searched using two methods; the linearization of the fitting function, and the gradient search [24]. Convergence of the fit was defined by a change in the normalized χ^2 of less than 10^{-4} in subsequent iterations. No significant differences in the extracted GDR parameters were found when fits were performed to data at individual angles, hence the angle-integrated center-of-mass spectra were used to improve the counting statistics, both for the singles and for the γ-multiplicity coincidence data. In the fitting process, the CASCADE calculated γ-ray spectrum was folded with the detector response function and then compared to the data.

A. Input parameters

In CASCADE the important input parameters which need to be specified include the level density, fusion cross section, spin distribution, yrast line, and the giant dipole and quadrupole resonance parameters.

1. Level density

The level density is assumed to have the same functional form as a free degenerate Fermi gas. Shell, pairing, and deformation effects are taken into account by introducing empirical parameters. We used the Reisdorf level density parametrization in which shell corrections are damped exponentially with excitation energy [25,23]. In this approach the level density parameters include the radius parameter r_0, the damping coefficient γ^{-1}, the pairing reference, and the liquid-drop model chosen to calculate the nuclear masses.

The radius parameter $r_0 \approx$ 1.09–1.13 fm for the mass 60 region was determined from electron scattering data [23]. In our fits we used the value r_0 = 1.127 fm which best reproduces the available experimental level spacing at low excitation energies $\leq$ 10 MeV for the mass 60 region, as can be seen in Fig. 3 of [23]. Although the level density is sensitive to the choice of the radius parameter r_0, small variations in r_0 do not change the calculated γ-ray spectra significantly. This is not surprising since the γ decay probability in the statistical model depends only on the ratio of the daughter nucleus level density reached

by γ-ray emission to that reached by particle emission. For the special case of $E_\gamma = \overline{E_{ev} + B}$, where $\overline{E_{ev} + B}$ is the average energy (kinetic + binding) removed by evaporation, this ratio should be independent of r_0. In general $E_\gamma \neq \overline{E_{ev} + B}$ and one expects a weak dependence on r_0. The GDR parameters extracted from fits to 175 MeV ^{32}S+^{27}Al data using different values of r_0 in the range of $\Delta r_0 = \pm 0.027$ fm results in $\pm 4\%$ change in the GDR strength and the width, and $\pm 2\%$ change in the centroid energy.

We used $\gamma^{-1} = 18.5$ MeV for the shell damping parameter, which was determined by empirical fit to data for masses 100–253 [25]. Schmidt *et al.* [26] have estimated this parameter from microscopic calculations and found it to be $\gamma^{-1} = 13.3$ MeV for ^{59}Cu. We found that the calculated γ-ray spectra are insensitive to the value chosen for this parameter except for a slight increase in the spectrum strength with increasing γ^{-1}. When fits were performed to the 175 MeV ^{32}S+^{27}Al data using these two values and an arbitrary larger value $\gamma^{-1} = 37$ MeV, the fit resulted in a 5% change in the extracted GDR strength, less than 3% change in the width, and no significant change in the centroid energy.

The pairing correction δ_p is calculated using the droplet model of Myers [27]. Using the odd-even nuclei as a reference this pairing correction is equal to $(\Lambda - \lambda)$, λ, or $(-\Lambda + \lambda)$ depending on whether the nucleus is odd-odd, odd-even, or even-even, where $\Lambda = 12/\sqrt{A}$, and $\lambda = -10/A$. Even-even or odd-odd pairing references can also be used; however, the calculated γ-ray spectrum was found to be insensitive to the chosen pairing reference. In all fits we used the odd-even pairing reference. The shell correction energy δ_s was determined from the difference of the experimental mass M_{expt} and the liquid-drop mass M_{LDM} such that $\delta_s + \delta_p = M_{expt} - M_{LDM}$. In CASCADE several liquid-drop models are available. The calculated δ_s differs significantly depending on the LMD used; however the shape of the γ-ray spectrum is basically insensitive to this choice. In all fits we used the Groote *et al.* LDM [28] including the Wigner term. The Wigner term must be included in order for the LDM to reproduce the nuclear symmetry energy deduced from energies of isobaric analog states [29]. The effect of including this term on the calculated γ-ray spectrum is small, and the extracted GDR parameters are unchanged except for about 4% decrease in the strength.

Calculations using the Pühlhofer level density approach [21] were also performed and compared with those conducted with the Reisdorf approach. When the level density parameter a, for the liquid-drop region in the Pühlhofer approach [21], is adjusted to give the same asymptotic $\tilde{a} = 6.9 = A/8.5$ as in the Reisdorf approach [25], the calculated γ-ray spectra using these prescriptions are similar.

2. *Fusion cross section*

The CASCADE code uses a simple relation to calculate the fusion cross section, which depends on the Coulomb barrier and on the sum of the radii of the two colliding nuclei. Instead of this estimate we used the fusion cross section obtained from measurements of evaporation residues. For ^{32}S+^{27}Al the fusion-evaporation residue excitation function has been measured over a wide range of projectile energies [13]. In Table II, we show the measured evaporation residue cross sections and the corresponding compound nucleus critical angular momenta.

Measurements of the fusion-evaporation cross section for the ^{18}O+^{45}Sc reaction were not found in the literature; however, this cross section has been measured for the nearby entrance channel ^{16}O+^{40}Ca [30,31], using measurements of evaporation residue mass and velocity distributions. We compared these cross sections to the predictions of CASCADE to obtain the ratios $\sigma_{fusion}(expt)/\sigma_{fusion}(CASCADE)$. Assuming that this ratio, at a given center-of-mass bombarding energy, is the same for both reactions, and using the CASCADE fusion cross section predictions for ^{18}O+^{45}Sc, an estimate of $\sigma_{fusion}(expt)$ for ^{18}O+^{45}Sc was obtained. This estimate is listed in Table II together with the corresponding l_0.

3. *Spin distribution*

For the inclusive measurements, we calculated the initial compound nucleus spin distribution in the smooth cutoff approximation based on the fusion cross sections given above. In the coincidence measurements, the fold ≥ 2 condition in the multiplicity filter leads to discrimination against low-spin reaction events, including low-spin compound nucleus formation. To account for this effect, we modified the initial spin distribution used in the CASCADE calculations. To obtain the modified spin distribution one must know the probability that for a given fold n in the multiplicity filter, a number M_γ γ rays are emitted. This probability distribution was calculated using a simple recursive formula [32]. The modified spin distribution for the fold ≥ 2 condition was then obtained assuming $J = 2$ M. This assumption ignores the angular momenta carried away by particle evaporation and hence leads to an overestimate of the effect of the fold ≥ 2 condition on the spin distribution. However, the effect of the fold ≥ 2 condition is not very big. This can be seen

TABLE II. Fusion-evaporation cross sections for ^{32}S+^{27}Al (measured) and ^{18}O+^{45}Sc (inferred, see text).

System	E_p (MeV)	$\sigma_{er}^{meas.}$ (mb)	l_0 ($\hbar$)	Ref.
^{32}S+^{27}Al	90	650 ± 65	24	[12]
	120	936 ± 94	34	[12]
	141	1073 ± 107	39	[13]
	175	1042 ± 104	43	[13]
	215	960 ± 96	45	[13]
^{18}O+^{45}Sc	52	946	26	[a]
	68	1240	35	[a]
	105	1027	39	[a]
	125	856	39	[a]
	149	742	39	[a]

[a]Inferred from ^{16}O+^{40}Ca measurements.

in Fig. 7, where we show the calculated spin distribution for $E_p = 175$ MeV, with and without the fold condition.

4. Yrast line

The yrast line is calculated using a spin-dependent moment of inertia approximated in CASCADE as $\theta = \theta_0(1 + \delta' J^2 + \delta'' J^4)$, where $\theta_0 = 2mR^2/5$ is the rigid-body moment of inertia with $R = r_0 A^{1/3}$. For the radius parameter r_0, we used the rms radius given by the droplet model calculation of Myers [27]. In all our calculations, the deformability parameters $\delta' = 2.10 \times 10^{-5}$ and $\delta'' = 1.59 \times 10^{-7}$ were used in order to reproduce the spin dependence of the moment of inertia calculated in the rotating liquid-drop model of Cohen, Plasil, and Swiatecki [1]. At high spins the RLDM predicts a shape transition from oblate to triaxial with rapidly increasing deformation. In Fig. 8(a), we show the RLDM moment of inertia θ/θ_0, as a function of spin, obtained from Fig. 11 of [1], with and without the oblate to triaxial shape transition (solid and dashed lines, respectively). The triaxial deformed shapes have a greatly increased moment of inertia which lowers the yrast line at high spins as shown in Fig. 8(b). The lowering of the yrast line enhances the phase space available for γ-ray and particle emission.

In attempting to understand the consequences of this enhancement, we performed CASCADE calculations for 175 MeV ^{32}S+^{27}Al with and without the oblate-to-triaxial shape transition in the moment of inertia, and obtained the partial widths for particle and γ-ray decays as a function of spin. For γ decay the effect of the shape transition in the moment of inertia is to increase the branching ratio at high spin. For $E_\gamma = 25$ and 17 MeV, the enhancement is up to a factor of 3 at $J = 40\hbar$ near the limit of compound nucleus formation, as shown in Figs. 8(c) and 8(d), respectively. For particle decay the shape transition enhances proton decay relative to alpha decay. This changes the Γ_α/Γ_p ratio, which is enhanced at moderate spin, back toward the values found at low spin, as can be seen in Fig. 8(e). This change in Γ_α/Γ_p is a direct consequence of the flattening of the yrast line. This effect, which was not appreciated in many studies of alpha particle spectra, has been shown to be important in understanding the measured spectra in terms of the statistical model [33].

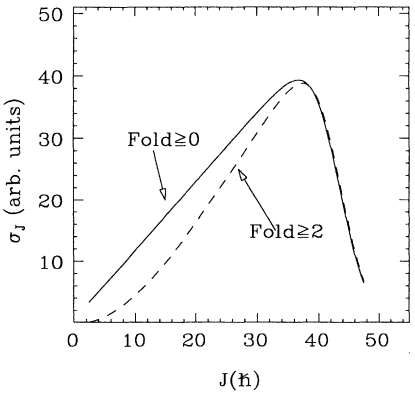

FIG. 7. Solid curve, initial spin distribution; dashed curve, effective initial spin distribution with a fold ≥ 2 coincidence condition, for 175 MeV ^{32}S+^{27}Al.

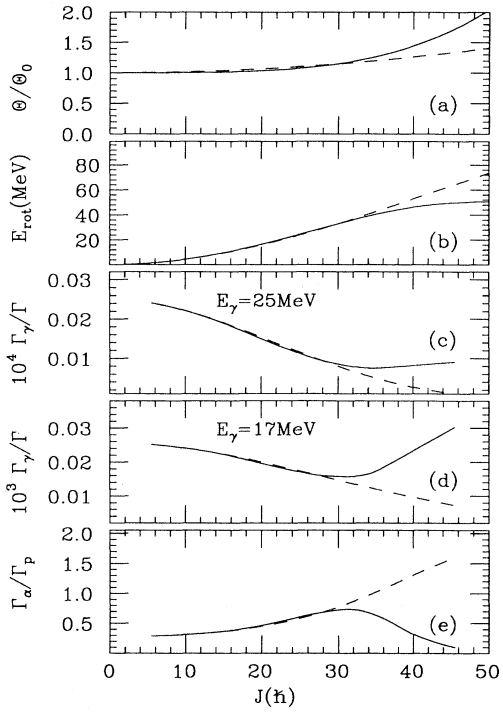

FIG. 8. (a) RLDM moment of inertia θ/θ_0, (b) calculated rotational energy, (c) calculated γ-ray branching ratio Γ_γ/Γ at $E_\gamma = 25$ MeV, and (d) at $E_\gamma = 17$ MeV, (e) calculated alpha to proton branching Γ_α/Γ_p vs spin, for first step decays of the initial CN. Solid curves, full RLDM; dashed curves, oblate-to-triaxial shape transition removed.

We performed CASCADE fits to the 175 MeV ^{32}S+^{27}Al spectrum shape, with and without the effect of the oblate-to-triaxial shape transition on the yrast line. The result is very similar GDR energies and widths, and a GDR strength that is 15% larger when the shape transition is included. These differences are too small to use to determine whether or not the shape transition has occurred.

5. Giant quadrupole resonance

Isoscalar (ISGQR) and isovector (ISVGQR) giant quadrupole resonances were included in the CASCADE fits. Each resonance was approximated by a Lorentzian with three fixed parameters, the strength (in units of an energy weighted sum rule), resonance energy, and width [4]. For the hot compound nuclei produced in our reactions, we determine the strength and the centroid energy for each resonance from the ground-state systematics [34], assuming that these parameters do not change

with temperature. The width on the other hand is assumed to increase with excitation energy, in analogy with the systematics of the GDR built on excited states. We used $S_{\rm IS} = S_{\rm IV} = 1.0$, $E_{\rm IS} = 16.3$ MeV, $E_{\rm IV} = 32.6$, and $\Gamma_{\rm IS} = \Gamma_{\rm IV} = 10.0$ MeV. The contribution from IVGQR decay in the GDR region of interest $12 \leq E_\gamma \leq 30$ MeV, is negligible and the contribution from the ISGQR is an order of magnitude smaller than the GDR. When fits are performed to the 175 MeV ^{32}S+^{27}Al data with both GQR components removed, the extracted GDR strength and width increase by 6 and 2%, respectively, with no significant change in the centroid energy.

B. Extracted GDR parameters

The CASCADE fits to the measured spectra are shown in Figs. 2 and 3 (solid curves) for ^{32}S+^{27}Al and ^{18}O+^{45}Sc systems, respectively. As noted above, a one-component GDR strength function was found to be sufficient to fit the data in the energy region $12.8 \leq E_\gamma \leq 30.0$ MeV for all the measured cases. The experimentally determined absorption cross sections $\sigma_{\rm abs}(E_\gamma)$ are discussed in Sec. V B and compared with the results of thermal fluctuation calculations. Values of the centroid energy, width, and total strength (in units of the classical dipole sum rule) determined from these fits for ^{59}Cu* and ^{63}Cu* nuclei are given in Table III. Errors in the GDR parameters, due to counting statistics and due to uncertainties in CASCADE input parameters, are added in quadrature. Systematic errors due to uncertainty in calculating the bremsstrahlung correction at the highest two bombarding energies of the ^{18}O+^{45}Sc reaction are estimated and quoted separately in a second error entry in Table III.

It is useful to present the GDR parameters determined from the fit results as a function of the final-state spin and temperature. For each bombarding energy, the average final-state spin $\bar{J}_f$ of the compound nucleus is calculated according to

$$\bar{J}_f = \frac{\sum_N \sum_{J_i^N} J_i^N \cdot \sigma_c(J_i^N) \cdot \Gamma_\gamma^N(J_i^N)/\Gamma^N(J_i^N)}{\sum_N \sum_{J_i^N} \sigma_c(J_i^N) \cdot \Gamma_\gamma^N(J_i^N)/\Gamma^N(J_i^N)} ,$$

where $\sigma_c(J_i^N)$ is the population cross section, and $\Gamma_\gamma^N(J_i^N)/\Gamma^N(J_i^N)$ is the branching ratio for emitting a γ ray with energy $E_\gamma = E_{\rm GDR} = 17$ MeV from a given nucleus N in the decay cascade, populated with initial spin J_i^N. In this estimate, we neglect the unit of angular momentum carried away by the dipole photon. The necessary quantities in the above equation were obtained by performing a series of CASCADE calculations at selected initial compound nucleus spins used to approximate the initial spin distribution. Similarly an average excitation energy $\bar{E}_x$ for γ decay with $E_\gamma = E_{\rm GDR} = 17$ MeV was obtained. The effective final-state temperature was calculated from the relation

$$\bar{T}_f^2 = \bar{E}_{xf}/a ,$$

where the mean final-state energy $\bar{E}_{xf} = \bar{E}_x - E_{\rm rot} - E_{\rm GDR}$, and $a = A/8$ MeV^{-1} is the approximate level

TABLE III. The GDR parameters determined from the CASCADE fits.

Reaction	E_p (MeV)	$\bar{J}_f$ ($\hbar$)	$\bar{T}_f$ (MeV)	$S_{\rm GDR}$	$E_{\rm GDR}$ (MeV)	$\Gamma_{\rm GDR}$ (MeV)	χ^2/ν	Comment
^{32}S+^{27}Al	90	12.8	1.7	0.9 ± 0.1	17.9 ± 0.4	9.1 ± 0.6	1.0	No MF condition
	120	17.6	1.8	0.9 ± 0.1	17.6 ± 0.3	9.7 ± 0.6	1.4	No MF condition
	141	22.0	1.9	1.0 ± 0.1	17.9 ± 0.3	11.7 ± 0.6	1.5	No MF condition
	175	27.5	2.0	1.1 ± 0.1	17.6 ± 0.4	13.5 ± 0.6	0.6	Fold ≥ 2
	175	27.5	2.0	1.2 ± 0.2	17.4 ± 0.3	13.6 ± 0.7	3.0	No MF condition
	215	31.5	2.1	1.1 ± 0.1	17.3 ± 0.4	13.4 ± 1.0	1.0	Fold ≥ 2
	215	31.5	2.1	1.1 ± 0.2	17.1 ± 0.3	14.4 ± 0.8	6.0	No MF condition
^{18}O+^{45}Sc	52	14.9	1.8	1.1 ± 0.2	17.3 ± 0.3	11.1 ± 0.6	1.6	No MF condition
	68	19.6	1.9	0.9 ± 0.1	17.3 ± 0.3	11.4 ± 0.6	1.3	No MF condition
	105	22.6	2.2	1.1 ± 0.1	16.8 ± 0.3	14.8 ± 0.9	1.2	No MF condition
	125	22.9	2.3	$1.1 \pm 0.1 \pm 0.2$	$16.7 \pm 0.3 \pm 0.1$	$12.7 \pm 0.7 \pm 2.2$	1.5	No MF condition [a]
	149	22.9	2.5	$1.2 \pm 0.1 \pm 0.2$	$16.5 \pm 0.3 \pm 0.1$	$13.0 \pm 0.7 \pm 2.0$	3.1	No MF condition [a]

[a] A bremsstrahlung correction was applied here.

density parameter. For all bombarding energies $\bar{J}_f$ is below the critical spin J_c (= $36\hbar$, and $39\hbar$ for ^{59}Cu and ^{63}Cu, respectively) for the oblate-to-triaxial shape transition predicted by the rotating liquid-drop model. However, the spin distribution extends well beyond J_c for the highest three bombarding energy ^{32}S+^{27}Al cases. For the 215 MeV ^{32}S+^{27}Al case for example, $\sim$ 30% of the cross section lies in the region $J \geq J_c$.

The extracted GDR strength and centroid energy, at all bombarding energies studied, are consistent with the ground state systematics ($S^{\text{g.s.}}_{\text{GDR}} = 0.97$ and $E^{\text{g.s.}}_{\text{GDR}} = 17.4$ MeV for ^{63}Cu [35]). On the other hand, the GDR width is much larger than the $\approx$ 5 MeV ground-state width. The GDR parameters determined from fits to the inclusive ^{32}S+^{27}Al data at the highest two projectile energies agree with the values determined from the fits to the exclusive data (fold $\geq$ 2 condition). This is consistent with the observation that the fold condition does not affect the GDR region of the spectrum. For ^{18}O+^{45}Sc, the width appears to saturate (within error bars) for $E_p \geq 105$ MeV. The central values for the widths at the highest two bombarding energies for this system are in fact narrower than that at lower $E_p = 105$ MeV; however, the systematic errors due to bremsstrahlung corrections in these two cases are large.

The GDR strength function is expected to become broader with increasing bombarding energy. This is because higher bombarding energies correspond to higher compound nuclear spins and temperatures. In the rotating liquid-drop model, the nuclear deformation is expected to increase with spin. The effect of deformation on the GDR is to split the strength function into different components, and increasing deformation leads to an increase in the size of this splitting. However, thermal fluctuations at finite nuclear temperature tend to smear out this splitting, and the combined effect of increasing spin and temperature is to make the GDR strength function broader. This qualitative expectation is in agreement with the increase of the GDR width observed in our data. Model calculations described in Sec. V predict that most of the increase in the GDR width arises from spin-driven increases in deformation. Our experimental results are consistent with the width increase being predominantly spin driven; however, it is difficult experimentally to separate the effects of spin and temperature.

C. Preequilibrium processes

In our statistical model analysis we have assumed that preequilibrium emission prior to fusion is negligible. The projectile and the target completely fuse to form a compound nucleus at an excitation energy equal to the total available energy of the system, and with an initial average angular momentum determined by the fusion-evaporated cross section. This is a crucial assumption that needs some elaboration.

In heavy-ion reactions at low bombarding energies, $E_p/A_p \leq 5$ MeV/nucleon, complete fusion (CF) dominates. However, at higher bombarding energies $E_p/A_p \geq 10$ MeV/nucleon, considerable experimental evidence exists for incomplete fusion (ICF) processes (e.g., [36]). In these processes preequilibrium particles are emitted at early stages of the collision so that only parts of the projectile or target fuse to form the compound nucleus. Such promptly emitted particles (PEP's) carry away energy, linear, and angular momenta. Therefore, the "compound nucleus" formed does not absorb the full linear momentum of the target and the projectile, and starts with only a portion of the total mass and energy of the entrance channel. The clearest experimental evidence for preequilibrium processes comes from charged particle emission measurements. In these measurements the statistical model calculations could not account for the high-energy part of the measured proton and alpha spectra and the extra yield is attributed to preequilibrium emission. The systematics of these measurements show that the multiplicity of the preequilibrium particles increases and the energy spectra become harder with increasing bombarding energy. For example, the multiplicity of high-energy protons with $E_p \geq 12$ MeV in ^{16}O+^{27}Al was found to increase from 0.15 at $E_p/A_p = 8.8$ MeV/nucleon to 0.65 at $E_p/A_p = 13$ MeV/nucleon [37]. Similarly the multiplicity of the high-energy α particles in ^{16}O+^{58}Ni was found to rise from less than 0.02 at $E_p/A_p = 6$ MeV/nucleon [38] to 1.0 at $E_p/A_p = 20$ MeV/nucleon [39].

Light charged particle emission spectra and angular distributions in ^{32}S+^{27}Al collisions were measured at bombarding energies similar to ours: E_p/A_p = 3–6.7 MeV/nucleon [40], and excellent agreement with statistical model calculations assuming complete fusion was reported. In these comparisons, no preequilibrium particle emission was needed to fit the data, suggesting that preequilibrium emission is small. The evaporation residue mass and velocity distributions were also measured over a wide range of bombarding energies for ^{32}S+^{27}Al. In this symmetric system the centroid of the velocity distribution is not sensitive to a possible incomplete fusion component but the width of the distribution is expected to get broader if preequilibrium particles are emitted. Both the measured velocity distributions and the measured evaporation residue mass distributions were found to be consistent with complete fusion up to $E_p = 320$ MeV [41], much higher than the projectile energies used in our work.

For ^{16}O+^{40}Ca, the reaction we used to infer complete fusion cross sections for our ^{18}O+^{45}Sc studies, there is evidence for some incomplete fusion. The analysis of [31] shows that at 140 MeV ^{16}O+^{40}Ca, which has the same $E_p^{\text{c.m.}}$ as 149 MeV ^{18}O+^{45}Sc, our highest bombarding energy case, incomplete fusion is about 25% of the complete fusion cross section. This corresponds roughly to an average preequilibrium particle emission multiplicity of 0.2, which we neglect.

V. THERMAL FLUCTUATION CALCULATIONS

A. Introduction

At finite temperature, thermal shape and orientation fluctuations affect the GDR observables, which are av-

eraged over all shapes experienced by the nucleus. To interpret our measured GDR spectra and angular distributions in terms of the shapes and shape evolution of the compound nuclei, comparison with thermal fluctuation calculations is necessary. In recent years, fluctuation calculations [42] of GDR decay of hot rotating nuclei have been developed [43–45]. In this theory, the hot rotating nucleus is described by a canonical ensemble of all possible nuclear deformations determined by the rotating liquid-drop free-energy surface (PES). In Fig. 9, we plot the PES contours for the ^{59}Cu nucleus at $E_x = 54$ MeV, calculated at different spins. Below the critical spin J_c ($= 39\hbar$ for the ^{59}Cu) the minimum of the PES, which corresponds to the equilibrium shape, lies along the oblate noncollective axis ($\gamma_0 = -180°$) with an equilibrium deformation β_0 which increases smoothly as the spin increases. At $J = J_c$, a shape change occurs. At higher spins the equilibrium shape is triaxial with γ_0 approaching the prolate collective axis ($\gamma = -120°$), and the deformation β_0 increasing rapidly with increasing spin. The minimum which was along the oblate noncollective axis for $J \leq J_c$ develops into a saddle point. This shape change, which is similar to the Jacobi shape transitions in gravitating rotating stars [46], is a second-order phase transition (in the limit of infinite nuclear matter), because the deformation parameters β_0 and γ_0, which correspond to the order parameters in the Landau theory of phase transitions [47], are continuous at $J = J_c$ while their derivatives are not.

A few features of this shape change are worth mentioning. As J approaches the critical spin J_c from below, the PES in the region of the minimum becomes increasingly soft along the decreasing $\beta\sin\gamma$ direction (the direction of the negative x axis of Fig. 9). The PES curvature κ_x along this direction decreases with increasing spin, approaching zero at the transition point. Beyond the transition point this softening is reversed, and κ_x increases with increasing spin. The curvature κ_y along the y axis ($y = \beta\cos\gamma$) continuously increases with increasing spin through the transition point. Above the transition point the deformation is large and the major to minor axis ratio approaches 2 and greater (corresponding to $\beta_0 \geq 0.7$).

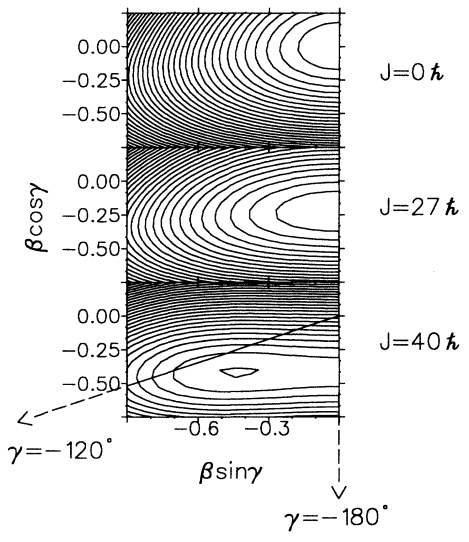

FIG. 9. Potential-energy surfaces (1 MeV contour intervals) for ^{59}Cu at $E_x = 54.4$ MeV at different spins. Below $J_c = 36\hbar$, the minimum lies along the oblate noncollective axis ($\gamma_0 = -180°$). Above $J = J_c$, the equilibrium shape is triaxial, γ_0 lies near the prolate collective axis ($\gamma = -120°$), and a saddle point lies on the oblate noncollective axis.

Fluctuation calculations of the GDR observables (the cross-section and angular distribution coefficients) were performed in the adiabatic approximation [43]. The GDR observables were first calculated at a given deformation and then averaged over all possible deformations. For each bombarding energy case, the calculations were further averaged over the spin distribution of the decaying nuclei, approximated by three-spin values. It should be pointed out that there are no free parameters in these calculations. The only parameters that enter the calculations are the zero-temperature GDR centroid energy, width, and the width scaling exponent δ which relates the widths of the different GDR components. The values $E_0 = 18$ MeV, $\Gamma_0 = 5.0$ MeV, and $\delta = 1.6$ were used.

B. Effective photoabsorption cross sections and comparison to calculations

Figures 10 and 11 (middle rows) show the experimentally determined absorption cross sections $\sigma_{\rm abs}(E_\gamma)$ for the ^{32}S+^{27}Al and ^{18}O+^{45}Sc reactions, respectively. The absorption cross section $\sigma_{\rm abs}(E_\gamma)$ was obtained by dividing the measured γ-ray cross section $\sigma_\gamma(E_\gamma)$ by, a statistical model "phase space," $\sigma_{\rm abs}(E_\gamma) = \sigma_\gamma(E_\gamma)/[\sigma_\gamma^{\rm fit}(E_\gamma)/\sigma_{\rm abs}^{\rm fit}(E_\gamma)]$, where $\sigma_\gamma^{\rm fit}(E_\gamma)$ is the least-squares CASCADE fit to the measured cross section, and $\sigma_{\rm abs}^{\rm fit}(E_\gamma)$ is the GDR absorption cross section determined from the fit. A fold ≥ 2 condition was required in the multiplicity filter for the 175 and 215 MeV ^{32}S+^{27}Al data shown here. The thick solid curves show the results of the shape and orientation fluctuation calculations. The calculations were performed for each bombarding energy case at three different spins, which approximate the spin distribution with equal weights, and then averaged. The corresponding PES for each spin is shown in the top rows of Figs. 10 and 11. Except for the highest spin increment in the $E_p = 175$ and 215 MeV ^{32}S+^{27}Al cases, all spins are below the Jacobi break point ($J_c = 36\hbar$ and $39\hbar$ for ^{59}Cu and ^{63}Cu, respectively).

The calculated absorption cross sections (thick solid curves) are in reasonable agreement with the data; in particular, the calculations correctly reproduce the observed broadening of the GDR width with increasing bombarding energy (spin). In the ^{18}O+^{45}Sc cases, the width of the calculated strength function increases with the average spin and then stays approximately constant once the average spin saturates at $\langle I\rangle = 23\hbar$, for $E_p \geq 105$ MeV.

C. Evidence for the Jacobi transition

So far in our comparisons, we have demonstrated how thermal fluctuation theory, in which nuclear spin and

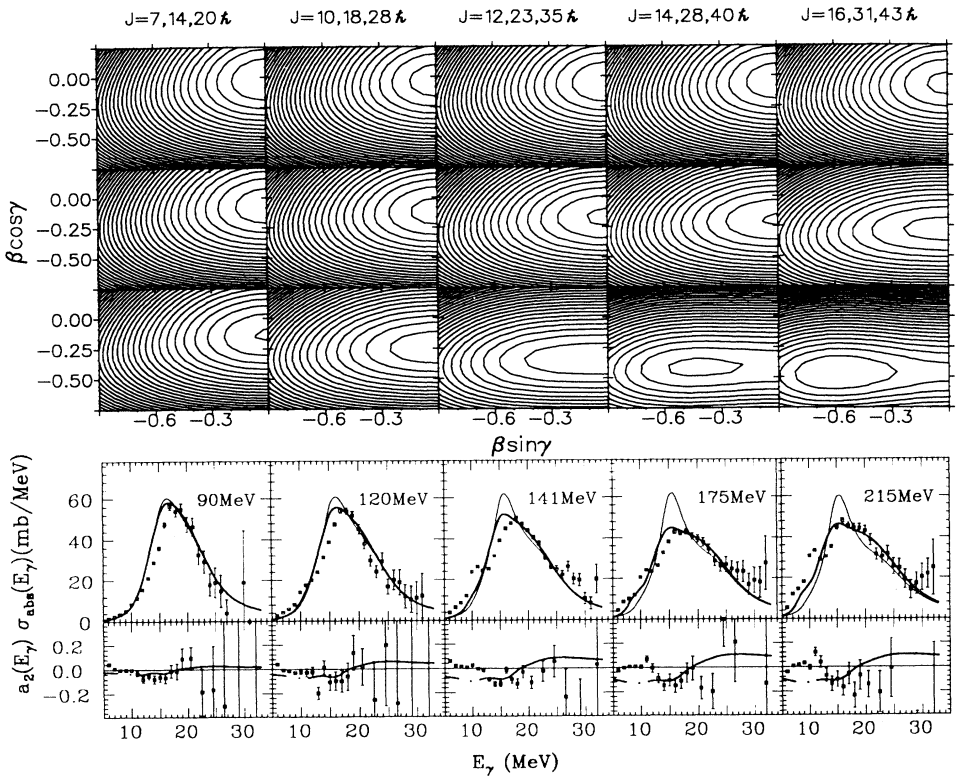

FIG. 10. $^{32}S+^{27}Al$. Bottom row: points, measured $a_2(E_\gamma)$ coefficients; thick solid curves, full fluctuation calculations. Middle row: points, $\sigma_{abs}(E_\gamma)$ inferred from measured cross sections and CASCADE fits; thick solid curves, fluctuation calculations with RLDM PES; light solid curves, fluctuation calculations with the shape transition removed. The calculated $\sigma_{abs}(E_\gamma)$ have been scaled by a factor of 0.9 in all cases. Top rows: RLDM potential-energy surfaces (1-MeV contour interval) for three different spins at each bombarding energy, with the lowest spin on top. 90, 120, and 141 MeV, inclusive data. 175 and 215 MeV, coincidence data (fold ≥ 2).

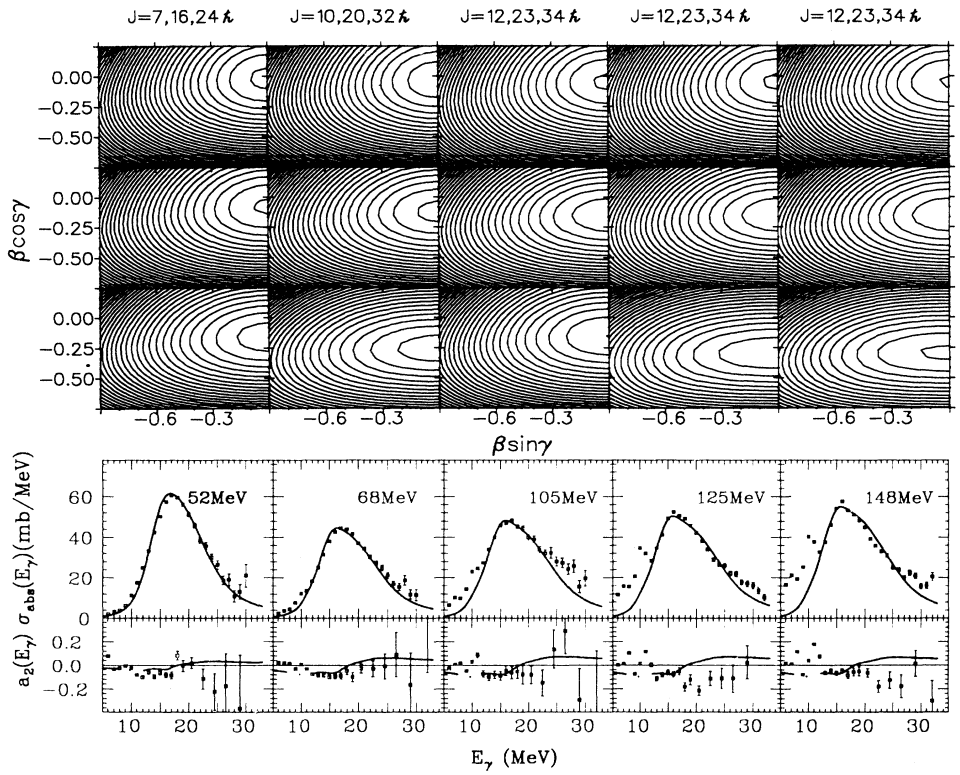

FIG. 11. $^{18}O+^{45}Sc$, as in Fig. 10 caption, except that here all data is inclusive. The calculated $\sigma_{abs}(E_\gamma)$ have been scaled by factors 0.9, 0.7, 0.8, 0.8, and 0.9, for the 52-, 68-, 105-, 125-, and 149-MeV cases, respectively.

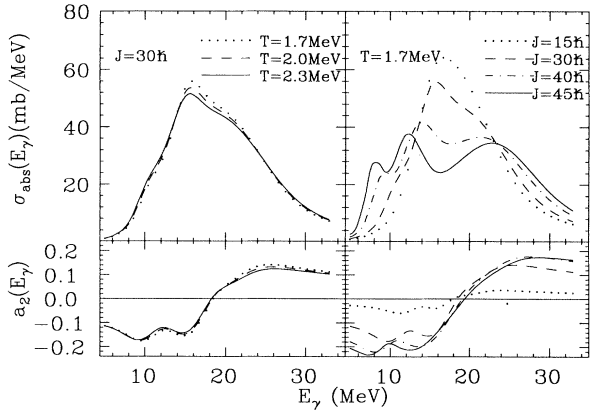

FIG. 12. Fluctuation calculations of $\sigma_{abs}(E_\gamma)$ (top row) and $a_2(E_\gamma)$ (bottom row) for decays of ^{59}Cu; left column, fixed spin ($30\hbar$) and varying T; right column, fixed temperature (1.7 MeV) and varying spin.

temperature effects are taken into account, can reproduce the measured GDR cross sections. To investigate further the separate effects of spin and temperature, we performed fluctuation calculations for ^{59}Cu in which the temperature is kept constant at $T = 1.7$ MeV, while the spin is varied. The calculated GDR cross section $\sigma_{abs}(E_\gamma)$ and angular distribution coefficient $a_2(E_\gamma)$ are shown in Fig. 12 (right column). At high spins, near the Jacobi transition ($J_c = 36\hbar$), the calculated spectral shape becomes much wider, and for spins above J_c it shows a pronounced structure. On the other hand, when the calculations are performed at constant spin ($J = 30\hbar$) and several temperatures $T = 1.7$, 2.0, and 2.3 MeV, the change in the calculated spectral shape is small as can be seen in Fig. 12 (left column). The calculated $a_2(E_\gamma)$ is not sensitive either to varying spin (except for very low spins), or to varying temperature, indicating that it provides little information on shape changes at very high spin.

To be more quantitative about the role played in the calculated spectral shapes by the predicted spin-induced Jacobi transition, fluctuation calculations were performed using potential-energy surfaces in which this shape change was removed. This was done by replacing the RLDM PES by a parabolic potential energy surface of the following form:

$$F(x,y) = \kappa_x(x-x_0)^2 + \kappa_y(y-y_0)^2 ,$$

where $x = \beta\sin\gamma$ and $y = \beta\cos\gamma$. At each spin, the minimum of this surface (x_0, y_0) was chosen to coincide with the actual RLDM minimum for $J < J_c$ and with the saddle point for $J > J_c$. The curvature κ_y was taken to be the same as that in the actual liquid-drop surface, while κ_x was set equal to its value at $J = 0$, in order to eliminate the x softness associated with the Jacobi transition. The shape and orientation fluctuation calculations of the absorption cross sections using these parabolic surfaces are shown as thin curves in Fig. 10 for ^{32}S+^{27}Al. As can be seen, the calculations with the Jacobi shape transition removed are adequate only at the lowest two bombarding energies, which correspond to low average spins. For the higher bombarding energy (spin) cases, these calculations fail to reproduce the experimental cross sections, indicating the importance of the Jacobi transition.

As mentioned above, an important feature of the Jacobi transition is the increased softness of the potential-energy surface in the $\beta\sin\gamma$ direction for spins below the transition break point J_c. This softness leads eventually to the transition and therefore acts as a precursor for it. The calculated spectral shapes are more sensitive to this softness than to the actual transition. This can be seen in Fig. 13, where $\sigma_{abs}(E_\gamma)$ for ^{32}S+^{27}Al is shown together with fluctuation calculations (thick solid curves) averaged over the spin distribution as in Fig. 10, and with fluctuation calculations performed at the median spin (thin solid curves). The median spin is less than J_c in all cases. The agreement of the data with the calculations performed at the median spins is good in all cases, including the 175- and 215-MeV cases. Since the actual spin distribution extends beyond J_c for 175 and 215 MeV, this comparison indicates that the calculated spectral shapes are mainly sensitive to the softness of the PES.

D. Comment on the adiabatic approximation

Our data provide one of several examples [4,5,45] in which the adiabatic theory of thermal fluctuations works well for describing measured GDR strength functions. In this theory, the shape degrees of freedom are assumed to equilibrate prior to CN decay, and the time scale t_c for fluctuations in the nuclear shape is assumed to be much longer than the time associated with the GDR frequency

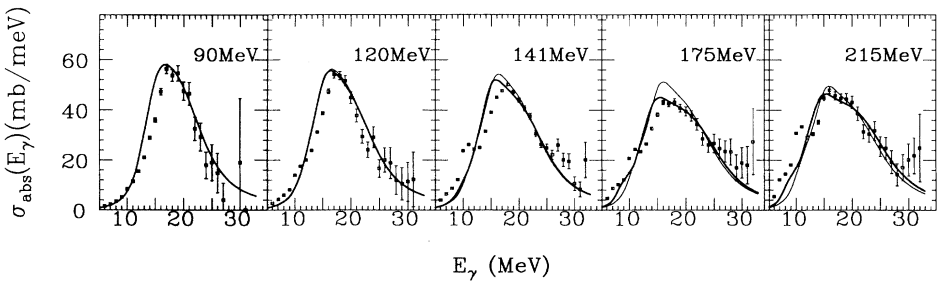

FIG. 13. Data points: $\sigma_{abs}(E_\gamma)$ derived from experiment as in Fig. 10; thick solid curves, $\sigma_{abs}(E_\gamma)$ from fluctuation calculations averaged over spin, as in Fig. 10; thin solid curves, fluctuation calculations performed at the median spin.

spread due to shape fluctuations ($\hbar/\Delta E$). Little is known about the relaxation time t_c. Studies of the GDR built on excited states can provide experimental information on t_c if the data is compared to a fluctuation theory in which dynamic effects are taken into account.

Although time-dependent fluctuation calculations of the GDR decay have not been performed for compound nuclei as light as $A \sim 60$, they have been performed in systems with $A \sim 108$ [48] and $A \sim 160$ [45]. In the work of Alhassid and Bush, the dynamics of the shape changes are described by a Langevin equation similar to the one for the motion of a heavy particle immersed in a fluid [49]. A damping parameter χ, which is related to t_c, is introduced, with large χ corresponding to large t_c (the adiabatic limit). For the case of ^{112}Sn at $T = 1.8$ MeV, $\chi = 125\hbar$ results in a GDR width (FWHM) which is about 20% less than the adiabatic limit (see Fig. 3 of [48]). Using the relation between χ and η given in [50], where η is the adiabaticity parameter, we estimate that the same deviation from adiabaticity (same η) in ^{59}Cu would correspond roughly to $\chi \approx 50\hbar$. Taking a 20% deviation in the width from the adiabatic limit to be the limit compatible with our experimental results, we arrive at a lower limit $\chi \geq 50\hbar$ for ^{59}Cu*. This limit could be improved upon by performing time-dependent fluctuation calculations for ^{59}Cu* and comparing to our experimental results.

Our limit for χ may be compared to theory. In the work of Bush *et al.* [51], the diffusion coefficient $D_\beta = T/\chi$ for quadrupole nuclear shape change is parametrized as $D_\beta \approx \alpha T^3/\varepsilon_f^2 A$ with $\alpha \sim 50$. Assuming that this relation is also valid in medium mass nuclei and taking $\varepsilon_f \approx 35$ MeV and $T = 2.0$ MeV, our $A = 59$ case implies $\alpha < 360$. Our upper limit on α is also compatible with other theory as shown in Table V of [51], but not with the results quoted there from prescission neutrons or from dipole narrowing data. However, it has been pointed out that this dipole narrowing estimate is not correct [52]. It should be mentioned that all estimates to date of the time scale for large amplitude shape change from GDR data assume equilibrium of the nuclear shape at time $t = 0$, an approximation which may not be good in all cases.

E. Calculations of $a_2(E_\gamma)$

The measured $a_2(E_\gamma)$ coefficients for the ^{32}S+^{27}Al and ^{18}O+^{45}Sc reactions, respectively, are shown in Figs. 10 and 11 (bottom rows) together with the thermal fluctuation calculation results (thick curves). A fold ≥ 2 condition is required in the multiplicity filter for the 175 and 215 MeV ^{32}S+^{27}Al data. The fold cut increases the statistical error bars on the $a_2(E_\gamma)$ coefficients by as much as a factor of 2 at high γ-ray energies, as can be seen in Fig. 14 where we compare $a_2(E_\gamma)$ measured with and without this fold condition.

The calculated $a_2(E_\gamma)$ agree with the data only in the region $12 \leq E_\gamma \leq 18$ MeV on the low-energy side of the giant dipole resonance. In particular, the observed negative dip around $E_\gamma \sim 16$ MeV, which increases in magnitude with bombarding energy, is reproduced. Below $E_\gamma \approx 12$ MeV, the data deviate substantially from the calculated curves, especially for the high bombarding energy cases. This deviation is not surprising for two reasons. First, a low E_γ nonstatistical background is observed both in the measured spectral shapes and in the angular distribution $a_1(E_\gamma)$ coefficients. Second, the statistical γ rays emitted in this energy region come predominantly from nuclei in the decay cascade formed after several particles have been emitted. These nuclei have lower spin and temperature than the nuclei which γ decay at higher E_γ, in the GDR region, and may be partially dealigned from the original direction. The average spins and temperatures used in the calculations are correct for the GDR region, but not for lower E_γ. In addition the effect of dealignment is not included.

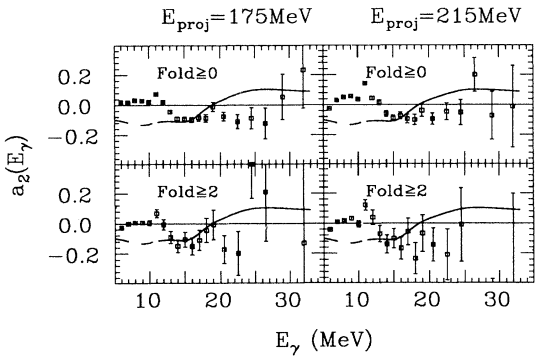

FIG. 14. $a_2(E_\gamma)$ coefficients for ^{32}S+^{27}Al at 175 MeV (left column) and 215 MeV (right column). Top row, inclusive data; bottom row, fold ≥ 2 condition. Solid curves, fluctuation calculations.

The discrepancies between the measured and calculated $a_2(E_\gamma)$ coefficients on the high-energy side of the GDR present a puzzling problem. Although the experimental statistics for the coincidence ^{32}S+^{27}Al data (Fig. 10) are too poor to judge, the singles data at high bombarding energy in both ^{32}S+^{27}Al (Fig. 14) and ^{18}O+^{45}Sc (Fig. 11) suggest that the negative $a_2(E_\gamma)$ values observed on the low side of the GDR persist on the high side. The fluctuation calculations of statistical GDR decay predict the $a_2(E_\gamma)$ coefficients should turn positive on the high-energy side of the resonance, in disagreement with the inclusive data at high bombarding energy. Although in the highest two bombarding energies of ^{18}O+^{45}Sc, a bremsstrahlung contribution at high E_γ is observed in the emission spectra and in the measured $a_1(E_\gamma)$ coefficients, the observed $a_2(E_\gamma)$ coefficients just above the GDR peak cannot be explained in terms of bremsstrahlung background. This is because the fractional bremsstrahlung contribution to the measured spectra, based on the analysis of $a_1(E_\gamma)$ described in Sec. III, increases by about a factor of 3 from $E_\gamma \approx 20$ to 30 MeV. This implies that the contribution to $a_2(E_\gamma)$ due to bremsstrahlung should also increase by this factor. However, in both cases the measured $a_2(E_\gamma)$ coefficients remains constant at $a_2(E_\gamma) \cong -0.15$ for $E_\gamma \geq 20$ MeV, indicating that the observed negative $a_2(E_\gamma)$ values in the region of the GDR peak are not due to bremsstrahlung.

Indeed, because the γ-ray intensity close to the GDR peak is so strong, it is unlikely that the observed negative $a_2(E_\gamma)$ can be due to anything other than GDR decay.

Negative $a_2(E_\gamma)$ coefficients can occur in the statistical emission of high-energy γ rays, even for a spherical nucleus, due to a level density effect [4]. This effect, which is not included in the fluctuation calculations, arises from the fact that the decay probability depends on the final-state level density, which is different for $\Delta I = 0$ and $\Delta I = \pm 1$. We have estimated this final-state level density effect and found it to be small ($a_2 \approx -0.017$ to -0.024 in the region $E_\gamma = 10$–30 MeV for the 175 MeV ^{32}S+^{27}Al case, estimated using $I = 29\hbar$), too small to account for the observed discrepancy at the high γ-ray energy region.

It is tempting to blame this discrepancy of a failure of the calculation. Indeed, Alhassid [43] has pointed out that the present fluctuation calculations, which are done in the approximation of constant spin (as opposed to constant rotational frequency), nonscalar observables such as $a_2(E_\gamma)$ are not determined with the same rigor as are scalar observables such as the cross section. Whether this limitation is relevant to the present problem remains to be seen.

VI. SUMMARY AND CONCLUSION

We have presented a systematic study of the GDR decays of ^{59}Cu and ^{63}Cu compound nuclei populated over a wide range of excitation energy and spin in the fusion of ^{32}S+^{27}Al and ^{18}O+^{45}Sc, respectively. The motivation was to search for the predicted spin-induced oblate-to-triaxial shape transition at very high spin. High-energy γ-ray production cross sections and angular distributions were measured. The measured angular distributions, in the CN center of mass, were found to exhibit forward-backward symmetry for $E_\gamma > 12$ MeV, in the GDR region of interest, for all ^{32}S+^{27}Al bombarding energies and for $E_p \leq 105$ MeV ^{18}O+^{45}Sc, supporting the compound nucleus decay hypothesis. For higher projectile bombarding energies in ^{18}O+^{45}Sc, the angular distributions were found to be forward peaked at high E_γ, and the angular distribution anisotropies have been used to deduce bremsstrahlung production cross sections at threshold.

Broad GDR strength functions were determined from statistical model fits to the measured spectral shapes at high bombarding energy (spin), implying the presence of large deformation in the ensemble of decaying states. The GDR strength functions are well described by thermal fluctuation calculations in which the GDR is averaged over a distribution of deformations determined from rotating liquid-drop model potential-energy surfaces. The calculations predict a substantial softening of the potential-energy surface at high spin, related to the equilibrium oblate-to-triaxial shape change, and the measurements are found to be sensitive primarily to this softening. The calculations fail to reproduce the experimental cross sections at high spin when the triaxial-to-oblate transition and the associated softness in the PES are removed, confirming that the observed broadening of the GDR strength function is mostly due to spin-driven deformation.

The calculated $a_2(E_\gamma)$ angular distribution coefficients are found to agree with the data only on the low-energy side of the resonance. Above the GDR centroid, discrepancies are observed between the calculations and the inclusive $a_2(E_\gamma)$ measurements at high bombarding energies (spins).

ACKNOWLEDGMENTS

This work was supported by the U.S. Department of Energy, Division of Nuclear Physics, at the University of Washington Under the Grant No. DF-FG06-90ER40537.

[1] F. Cohen, F. Plasil, and W. Swiatecki, Ann. Phys. (NY) **82**, 557 (1974).
[2] M. G. Mustafa, P. A. Baisden, and H. Chandra, Phys. Rev. C **25**, 2524 (1982).
[3] A. J. Sierk, Phys. Rev. C **33**, 2039 (1986).
[4] K. A. Snover, Annu. Rev. Nucl. Part. Sci. **36**, 545 (1986).
[5] J. J. Gaardhoje, Annu. Rev. Nucl. Part. Sci. **42**, 483 (1992).
[6] M. Kicinska-Habior, K. A. Snover, J. A. Behr, C. A. Gossett, Y. Alhassid, and N. Whelan, Phys. Lett. B **308**, 225 (1993).
[7] J. H. Gundlach, K. A. Snover, J. A. Behr, C. A. Gossett, M. Kicinska-Habior, and K. Lesko, Phys. Rev. Lett. **65**, 2523 (1990).
[8] R. E. Marrs, E. G. Adelberger, and K. A. Snover, Phys. Rev. C **16**, 61 (1977).
[9] H. Glatzel, Diplom thesis, University of Washington, 1986.
[10] D. Ye, Z. M. Drebi, M. S. Kaplan, M. Kelly, K. A. Snover, and D. P. Wells, Nucl. Phys. Lab. Annual Report, 1993, p. 83.
[11] F. Porto, S. Sambataro, K. Kusterer, L. K. Pao, G. Doukellis, and H. L. Harney, Nucl. Phys. **A357**, 237 (1981).
[12] H. H. Gutbrod, W. G. Winn, and M. Blann, Nucl. Phys. **A213**, 267 (1973).
[13] G. Doukellis, G. Hlawatsch, B. Kolb, A. Miczaika, G. Rosner, and B. Sedelmeyer, Nucl. Phys. **A485**, 369 (1988).
[14] G. Rosner, G. Hlawatsch, B. Kolb, G. Doukellis, J. B. Natowitz, and Th. Walcher, Nucl. Phys. **A385**, 174 (1982).
[15] D. Pelte, U. Winkler, R. Novotny, and H. Gräf, Nucl. Phys. **A371**, 454 (1981).
[16] C. Agodi *et al.*, Z. Phys. A **340**, 341 (1991).
[17] C. Agodi *et al.*, Phys. Lett. B **308**, 220 (1993).
[18] W. Cassing, V. Metag, U. Mosel, and K. Niita, Phys. Rep. **188**, 364 (1990).
[19] C. A. Gossett, J. A. Behr, S. J. Luke, B. T. Mclain, D. P. Rosenzweig, and K. A. Snover, Phys. Rev. C **42**, R1800 (1990); N. Gan, K.-T. Brinkmann, A. L. Caraley, B. J. Fineman, W. J. Kernan, R. L. McGrath, and P. Danielewicz, *ibid.* **49**, 298 (1994); R. J. Vojtech, R.

Butsch, V. M. Datar, M. G. Herman, R. L. McGrath, P. Paul, and M. Thoennessen, *ibid.* **40**, R2441 (1989).
[20] F. Ajzenberg-Selove, Nucl. Phys. **A506**, 64 (1990).
[21] F. Pühlhofer, Nucl. Phys. **A280**, 267 (1977).
[22] M. N. Harakeh, D. H. Dowell, G. Feldman, E. F. Garman, R. Loveman, J. L. Osborne, and K. A. Snover, Phys. Lett. B **176**, 297 (1986); J. A. Behr, Ph.D. thesis, University of Washington, 1991; and private communication.
[23] M. Kicinska-Habior, K. A. Snover, J. A. Behr, G. Feldman, C. A. Gossett, and J. H. Gundlach, Phys. Rev. C **41**, 2075 (1990).
[24] P. R. Bevington, *Data Reduction and Error Analysis for the Physical Sciences* (McGraw-Hill, New York, 1969).
[25] W. Reisdorf, Z. Phys. A **300**, 227 (1981).
[26] K.-H. Schmidt, H. Delagrange, J. P. Dufour, N. Carjan, and A. Fleury, Z. Phys. A **308**, 215 (1982).
[27] W. Myers, At. Data Nucl. Data Tables **17**, 411 (1976).
[28] H. Groote, E. R. Hilf, and K. Takahashi, At. Data Nucl. Data Tables **17**, 418 (1976).
[29] J. A. Behr, K. A. Snover, C. A. Gossett, M. Kicinska-Habior, J. H. Gundlach, Z. M. Drebi, M. S. Kaplan, and D. P. Wells, Phys. Rev. Lett. **70**, 3201 (1993); J. A. Behr, Ph.D. thesis, University of Washington, 1991.
[30] S. Vigdor, D. Kovar, and P. Sperr, Phys. Rev. C **20**, 2147 (1979).
[31] C. Beck, D. G. Kovar, S. J. Sanders, B. D. Wilkins, D. J. Henderson, and R. V. F. Janssens, Phys. Rev. C **39**, 2202 (1989).
[32] A. Maj, J. J. Gaardhoje, A. Atac, S. Mitarai, J. Nyberg, A. Virtanen, A. Bracco, F. Camera, B. Million, and M. Pignanelli, Nucl. Phys. **A571**, 185 (1994); A. Maj, private communication.
[33] J. R. Huizenga, A. N. Behkami, I. M. Govil, W. U. Schröder, and J. Tőke, Phys. Rev. C **40**, 668 (1989).
[34] F. E. Bertrand, Annu. Rev. Nucl. Sci. **26**, 457 (1976).
[35] M. Kicinska-Habior, K. A. Snover, C. A. Gossett, J. A. Behr, G. Feldman, H. Glatzel, and J. H. Gundlach, Phys. Rev. C **41**, 2075 (1990).
[36] H. Morgenstern, W. Bohne, W. Galster, K. Grabisch, and A. Kyanowski, Phys. Rev. Lett. **52**, 1104 (1984).
[37] T. C. Awes, S. Saini, G. Poggi, C. K. Gelbke, D. Cha, R. Legrain, and G. D. Westfall, Phys. Rev. C **25**, 2361 (1982).
[38] H. Ho *et al.*, Phys. Rev. C **27**, 584 (1983).
[39] P. L. Gonthier, H. Ho, M. N. Manboodiri, J. B. Natowitz, L. Adler, S. Simon, K. Hagel, S. Kniffen, and A. Khodai, Nucl. Phys. **A411**, 289 (1983).
[40] B. Fornal, G. Prete, G. Nebbia, F. Trotti, G. Viesti, D. Fabris, K. Hagel, and J. B. Natowitz, Phys. Rev. C **37**, 2624 (1988); R. K. Choudhury, P. L. Gonthier, K. Hagel, M. N. Namboodiri, J. B. Natowitz, L. Alder, S. Simon, S. Kniffen, and G. Kerkowitz, Phys. Lett. **143B**, 74 (1984).
[41] G. Rosner, J. Pochodzalla, B. Heck, G. Hlawatsch, A. Miczaika, H. J. Rabe, R. Butsch, B. Kolb, and B. Sedelmeyer, Phys. Lett. **150B**, 87 (1985).
[42] M. Gallardo, M. Diebel, T. Dφssing, and R. Broglia, Nucl. Phys. **A443**, 415 (1985).
[43] Y. Alhassid and N. Whelan, Nucl. Phys. **A565**, 427 (1993).
[44] Y. Alhassid and B. Bush, Nucl. Phys. **A531**, 39 (1991).
[45] Y. Alhassid and B. Bush, Nucl. Phys. **A509**, 461 (1990).
[46] Chandrasekhar, *Ellipsoidal Figures of Equilibrium* (Yale University Press, New Haven, CT, 1969).
[47] L. D. Landau and E. M. Lifshitz, *Statistical Physics* (Pergamon, Oxford, 1980), Part 1.
[48] Y. Alhassid and B. Bush, Phys. Rev. Lett. **63**, 2452 (1989).
[49] Y. Alhassid and B. Bush, Nucl. Phys. **A514**, 434 (1990).
[50] Y. Alhassid and B. Bush, Nucl. Phys. **A531**, 1 (1991).
[51] B. W. Bush, G. F. Bertsch, and B. A. Brown, Phys. Rev. C **45**, 1709 (1991).
[52] K. A. Snover, in *Future Directions in Nuclear Physics with 4 π Gamma Detection Systems of the New Generation*, edited by J. Dudek and B. Haas, AIP Conf. Proc. No. 259 (AIP, New York, 1992), p. 299.